Laser Beam Steering Along 3D Paths

B. Tamadazte, *IEEE Member*, R. Renevier, J.-A. Seon, A. V. Kudryavtsev, and N. Andreff, *IEEE Member*

Abstract— This paper deals with the development of a vision-based control scheme for 3D laser steering. It proposes to *incorporate* a simplified trifocal constraint inside a path following scheme in order to ensure intuitively a 3D control of laser spot displacements in unknown environment (target). The described controller is obtained without complex mathematical formulation nor matrix inversion as it requires only weak camera and hand-eye calibration.

The developed control law was validated in both simulation and experimental conditions using various scenarios (e.g., static and deformable 3D scenes, different control gains, initial velocities, etc.). The obtained results exhibit good accuracy and robustness with respect to the calibration and measurement errors and scene variations. In addition, with this kind of laser beam steering controller, it becomes possible to perfectly decouple the laser spot velocity from both the path shape and time. These features can fit several industrial applications (welding, micromachining, etc.) as well as surgical purposes (e.g., laser surgery) requirements.

I. INTRODUCTION

Reliable laser beam steering is very useful in several applications: i) industrial, e.g., regular welding [1], laser engraving machines [2], optical data storage and information display, free-contact micromanipulation, etc., ii) medical (laser surgery) [3], e.g., ophthalmology, neurosurgery, phono-surgery [4], etc., and iii) distance measurements e.g., laser rangefinder [5], mobile robotic navigation, etc. Then, to be able to ensure a reliable (accurate, stable and robust) laser beam steering, at least, two of the following elements are required:

- a laser scanning mechatronic system, e.g., electrical motors, galvanometers, robotic arms, piezoelectric or magnetostrictive actuators [6]–[8],
- a control law scheme which nowadays tends to be based on visual/optical feedback [9], [11], [12] or other efficient control schemes [10].

This paper focuses on the second point which concerns the development of a vision-based control scheme which must ensure the control, in a closed-loop scheme, of the laser beam (respectively, laser spot) motion. In the literature, the most referenced methods for laser beam (respectively, laser spot) steering were based on open-loop control schemes [13]. Consequently, to respect the laser steering specifications (e.g., accuracy, robustness), the scanning device must be

accurately modelled (geometric, optical and modelling) and even calibrated (compensation of the different mechanical imperfections of the mirror/prism mechanism) [14]. On the other hand, closed-loop approaches are generally based on the use of vision feedback, such as trajectory tracking [9], [15], path following [11], [14], [16], and point-to-point methods [19].
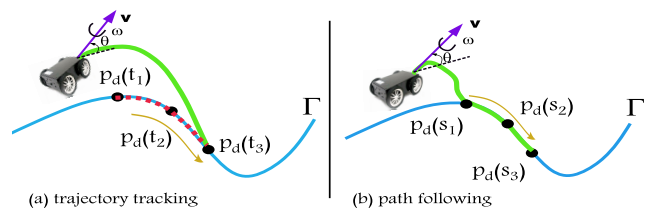
Fig. 1. Trajectory tracking *versus* path following.

Path following in mobile robotics has been widely studied in the literature for many years and has found several applications in the industrial fields (e.g., autonomous vehicle control, farming application). Path following differs from trajectory tracking essentially by the fact that the notion of "*time*" is removed in the first one (Fig. 1). Indeed, a typical motion control problem in trajectory tracking concerns the design of control laws that force a robot to reach and follow a time-parameterized reference (i.e., a geometric path with an associated time law). On the other hand, in path-following scheme, the robot is required to converge and track a path that is specified without time constraints. This makes possible to easily tune the velocity according to the task to be performed.

In path following, we assume that the robot's forward velocity tracks a desired speed profile, while the path following controller acts on the robot's orientation to drive it to the desired curve. It has been demonstrated that path following methods allow a smoother convergence to the desired curve and present less saturation within the controller comparing to trajectory tracking approaches. In addition, as shown by Brockett [20], mobile robots are not stable with continuous steady state feedback laws (e.g., unstable zero-dynamics). This problem can be tackled using a chained system to design the controller with an exact linearization as demonstrated by Morin and Samson [18] using a path following scheme. Therefore, the path following problem can be divided into two sub-tasks:

- a geometric task, which consists of approaching the robot to the desired curve,
- a dynamic assignment task, which assigns a velocity profile (instead of time) to the desired curve.

Our work goes beyond the state-of-the-art on both mobile robot and laser path following methods. In fact, we developed a new path following paradigm able to work efficiency with non-parametrized 3D curves. This becomes possible thanks the introduction of the trifocal geometry proprieties into the control scheme. In other words, we take into account *intuitively* the scene depth Z in new 3D path following method without any prior knowledge or estimation of the observed scene (e.g., 3D reconstruction) thanks to the trifocal constraint. In opposition to the conventional trifocal system, our three-view system was built using two real cameras (a stereovision system) and *one virtual camera made by a pan-tilt mirror which grabs one pixel at a time*. A first investigation of this concept was treated in [19] in which the theoretical bases were laid and a proof of stability was demonstrated in a planar scene.

This paper claims several contributions, among them are:

- development of a robust and accurate path following method able to operate in non-parametrized 3D curves (with keeping an uniform velocity along the path);
- combining a new formulation of the well-known trifocal constraint with the 2D kinamatic model of the path following to take into account the scene depth without any prior knowledge of the scene (e.g., 3D reconstruction, Z estimation method, etc.).
- requiring only rough estimation of calibration parameters (camera and hand-eye calibration);
- avoiding manipulations with complex and time-consuming mathematical expressions (e.g., matrices and tensors inversion);
- ability to work with static and deformable scenes without any adaptation of the control method.

In practice, the paper also implements automatic stereoscopic matching in order to allow the user to define the control trajectory in a single image and retrieve automatically this trajectory in the second image. Finally, the proposed methods were successfully validated in simulation in favourable and unfavorable working conditions (rough calibration, measurements noise, etc.). Also, an experimental set-up (miming the simulator) was built allowing a real environment validation. Through the different performed tests and the obtained results, it can be stated that the developed methods are accurate and robust meeting the industrial and medical requirements in the field of laser steering.

In the remainder of this paper, Section II reminds the basics of the 2D path following control law as well as the trifocal geometry principles. Section III deals with the design of our control law for laser steering along unknown 3D paths while Section IV presents the different simulation validations (in favorable and unfavorable conditions of use) in both static and deformable 3D scenes. The proposed methods were also successfully validated using a home-made experimental set-up as reported in Section V.

II. BACKGROUND

This section deals with some background on the path following principles as well as the basics of three-view geometry. Therefore, we start with the introduction of the well-known 2D path following controller.

A. Reminders on the 2D Path Following
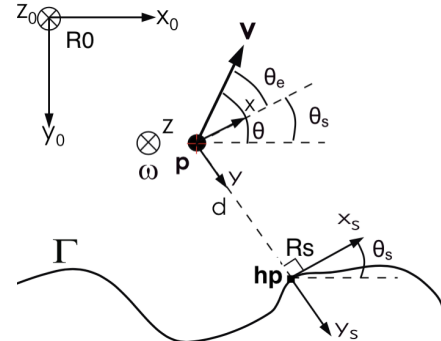
Fig. 2. Representation of the *Frénet* frame and the image frame.

First, in our previous work [11], we have demonstrated that the laser spot path following in the image plane (2D) is very similar to the one of an unicycle operating on the ground [18]. For instance, in both cases, the direction and the velocity magnitude are servoed independently. In addition, in case of unicycle, the curvilinear velocity is expected to be constant, and in the same manner, the velocity of laser spot displacement on the target needs to be constant in laser steering.

In practice, the movement of the laser spot on the image plane is ensured by the control of a pan-tilt mirror on which the laser beam is reflected. The path to be tracked consists of a non-parameterized curve Γ sampled into a set of 2D points $a_1, a_2, \cdots, a_N$ (each point has as Cartesian coordinates $(x_{a_i}, y_{a_i})^\top$) (Fig. 3).

Thus, let us consider that the laser spot is defined by a 2D image point $p = (x, y)^\top$ linked to the image frame $\mathcal{R}_0$. Recall that, the kinematic model of the laser spot is similar to the unicycle one. Therefore, the laser spot position, represented in the *Frénet* frame $\mathcal{R}_s$ (Fig. 2), is expressed by the following kinematic system of equations [11]

$$\dot{s} = \frac{v}{1 - dC(s)} \cos\theta_e \quad (1)$$

$$\dot{d} = v\sin\theta_e \quad (2)$$

$$\dot{\theta}_e = \omega - \dot{s}C(s) \quad (3)$$

where s and $C(s)$ are the curvilinear abscissa and the curvature, respectively. The angle θ_e is the difference between the laser velocity $\mathbf{v}$ direction and the tangential vector x_s in the frame $\mathcal{R}_s$, d is the shortest distance between p to Γ, $v = \dot{p}$ represents the translational velocity magnitude of the laser spot p while $\omega = \dot{\theta}$.

Furthermore, the control of the laser spot motion is confined to the task of maintaining the distance d and the orientation error θ_e equal to 0.

The path following method requires to compute the translational velocity direction $\mathbf{v}$ and the rotational one ω at each

iteration i. Note that the position of the laser spot p and the curvilinear coordinates s and $C(s)$ are computed at each iteration (please see Section II-B for the implementation details). Thereby, the two control inputs used to control the laser spot motion, namely rotational velocity ω and the tangential velocity $\mathbf{v}$ are obtained by the following expressions, respectively (please see [11] for more details)

$$\omega = \frac{u_2 + \left(\dot{d}C(s) + d\frac{\partial C(s)}{\partial s}\dot{s}\right)\tan\theta_e}{\left(1 - dC(s)\right)\left(1 + \tan^2\theta_e\right)} + \dot{s}C(s) \quad (4)$$

and

$$\mathbf{v} = v.\mathbf{x}_s \quad (5)$$

B. Details on the Implementation of the 2D Path Following

In practice, p (the current laser spot position expressed in the image frame $\mathcal{R}_0$) is computed over time through a dot visual tracking algorithm, d is computed as $d = (p - h_p).\mathbf{y}_s$ (Fig. 2), and the angle $\theta_e = \arctan 2(v.\mathbf{x}_s, v.\mathbf{y}_s)$. Note that $\dot{s}$, $\dot{d}$ and $\dot{\theta}_e$ are obtained by a simple numerical differentiation between two successive iterations i and $i + 1$.

To compute the curvilinear coordinates s as well as $C(s)$, we use the following methodology. First, s is obtained as follows

- if $i = 1$, then
$$s(1) = 0$$

- else if $i \neq 1$,
$$s(i+1) = s(i) + \sqrt{\left(x(i+1) - x(i)\right)^2 + \left(y(i+1) - y(i)\right)^2}$$

Secondly, the curvature $C(s)$ can be approximated by the inverse of the radius of Γ at each point a_i i.e., $C(s) = \frac{1}{r}$. So, the radius r is obtained using each three successive points (a_{i-1}, a_i, a_{i+1}) on Γ as shown in Fig. 3.
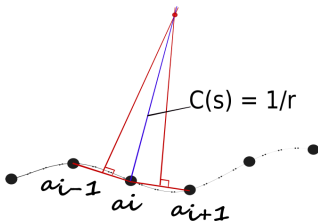
Fig. 3. Illustration of the estimation of $C(s)$ at each iteration i.

Condition: *as the curvature $C(s)$ needs to be computed for the control law (see equation (4)), the curve to be tracked has to be at least C^2 ($C(s)$ is the time-derivation of the tangent vector).*

Finally, the expression for the new velocity direction is obtained by combining the current velocity direction and the rotational one. Thereby,

- if $i = 1$, then
$$\mathbf{v}_0 = v.\mathbf{x}_s \quad (6)$$

where v is the initial velocity value (defined by the operator), and $\mathbf{x}_s$ is the tangential vector to the path Γ (Fig. 2). Note that, the higher the velocity v the faster the laser spot reaches Γ.

- else if $i \neq 1$,
$$\mathbf{v}_{i+1} = \frac{\mathbf{v}_i + \omega \times \mathbf{v}_i}{\|\mathbf{v}_i + \omega \times \mathbf{v}_i\|} \quad (7)$$

where $\times$ defines the cross-product and $\mathbf{v}_i$ represents the current velocity vector of the laser spot.

Stability conditions: *the controller is asymptotically stable when*
- *v is a bounded differentiable time-function;*
- *v does not tend to zero when t tends to infinity;*
- *$\dot{v}$ is bounded.*

Note that at this stage, the laser steering control law is able to work only for 2D curves (e.g., on planar surfaces) due the fact that the scene depth Z does not appear in the control inputs $\mathbf{v}$ and ω. Consequently, when it concerns 3D surfaces as well as deformable scenes (time-variation of Z), as it is the case in industrial and medical applications, it is necessary to introduce the notion of depth in the control law expression. This issue will be addressed in the following, namely, by introducing the three-view geometry proprieties in the control inputs.

C. Revisited Three-View Geometry
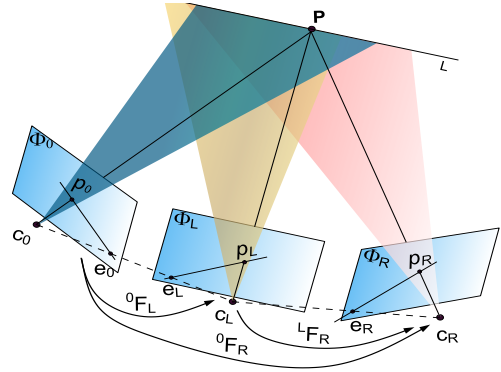
Fig. 4. The three-view geometry.

A three-view vision system is generally modelled using a $3 \times 3 \times 3$ array tensor also known as *trifocal tensor*. It embeds the projective geometric relationships in a three-view system. This means that it is possible to link the coordinates of corresponding points $p_i = (x_i, y_i)^\top$ or lines (l_i) in the other views independently from the scene structure, but using only the relative cameras' poses. Trifocal tensor can be *considered* as the equivalent to the fundamental matrix in stereovision. For instance, R. Hartley and A. Zisserman, in [21], have defined the point-point-point transformation as follows

$$[\tilde{p}_L]_\times \left(\sum_{i=1}^{3} \tilde{p}_0 \mathbf{T}_i\right) [\tilde{p}_R]_\times = 0_{3\times3} \quad (8)$$

where $[\tilde{p}_i]_\times$ is the skew-symmetric matrix associated to the vector cross-product $\times$ by $\tilde{p}_i$. The latter is the homogeneous representation of an image point i.e., $\tilde{p}_i = (p_i, 1)^\top$. The concatenation of the three 3×3 matrices i.e., $\mathbf{T}_1$, $\mathbf{T}_2$, and $\mathbf{T}_3$ defines the trifocal tensor $\mathcal{T}_{3\times3\times3}$.

Fig. 5. Overview of three-view system including two real cameras and a laser source (virtual camera).

One can remark that the formula (8) is generally inappropriate for the design of control laws because it involves several complex matrix (respectively, tensors) manipulations, numerical approximations and matrices and tensors inversions [22]. As a result, we have revisited the trifocal constraint by making an analogy between a three-camera system and a two-camera + laser scanner system [19]. As shown in Fig. 5, it is possible to consider that the third view as a *virtual image* made by a pan-tilt laser scanner which grabs one pixel at a time. Consequently, it becomes possible to write the following system of equations

$$\tilde{p}_{\mathrm{L}}^{\;\top}\,{}^{\mathrm{L}}\mathbf{F}_{\mathrm{R}}\,\tilde{p}_{\mathrm{R}} = 0 \tag{9}$$
$$ {}^{0}\underline{\mathbf{n}}^{\top}\,{}^{0}\mathbf{F}_{\mathrm{R}}\,\tilde{p}_{\mathrm{R}} = 0 \tag{10}$$
$$ {}^{0}\underline{\mathbf{n}}^{\top}\,{}^{0}\mathbf{F}_{\mathrm{L}}\,\tilde{p}_{\mathrm{L}} = 0 \tag{11}$$

where ${}^{i}\mathbf{F}_j$ is the fundamental matrix between the camera i and j, and ${}^{0}\underline{\mathbf{n}}$ defines the laser beam orientation which passes through $\tilde{p}_0$ (Fig. 5).

In fact, the projection of the 3D point $\mathbf{P}$ on the virtual image gives $\tilde{p}_0$. This projection can be written as $\mathbf{P} = Z\tilde{p}_0$. One can note that the distance Z is the depth which means the distance parallel to the virtual optical axis (carried by the vector ${}^{0}\underline{\mathbf{n}}$). Also, it has to be underlined that ${}^{0}\underline{\mathbf{n}}$ and $\tilde{p}_0$ are projectively similar, i.e., ${}^{0}\underline{\mathbf{n}} \equiv \tilde{p}_0$. The latter can explain the system of equation above).

As a result, the equations (9), (10), (11) can be reformulated in a ***simplified trifocal constraint*** as follows

$${}^{0}\underline{\mathbf{n}} \times \left({}^{0}\mathbf{F}_{\mathrm{R}}\,\tilde{p}_{\mathrm{R}} \times {}^{0}\mathbf{F}_{\mathrm{L}}\,\tilde{p}_{\mathrm{L}}\right) = 0 \tag{12}$$

which is equivalent to the point-point-point trifocal tensor (8).

In addition, by the introduction of the following notations $\mathbf{h}_{\mathrm{L}} = {}^{0}\mathbf{F}_{\mathrm{L}}\,\tilde{p}_{\mathrm{L}}$ and $\mathbf{h}_{\mathrm{R}} = {}^{0}\mathbf{F}_{\mathrm{R}}\,\tilde{p}_{\mathrm{R}}$ (for more details please refer to our previous work [19]) which represents the normal vectors

to the view planes of the left image $\mathbf{I}_{\mathrm{L}}$ and the right image $\mathbf{I}_{\mathrm{R}}$, respectively (Fig. 5), it becomes possible to write

$${}^{0}\underline{\mathbf{n}} \times \left(\mathbf{h}_{\mathrm{R}} \times \mathbf{h}_{\mathrm{L}}\right) = 0 \tag{13}$$

Remark 1: *it is important to underline that in this new formula, the trifocal constraint is obtained by only a double cross-product of 3 vectors, instead of the traditional $3\times3\times3$ tensor. This new formulation is more suitable for the design of three-view geometry-based control law.*

The time-differentiation of (13) allows linking the laser beam angular velocity to the variations of the normal vectors $\mathbf{h}_{\mathrm{L}}$ and $\mathbf{h}_{\mathrm{R}}$ to the image planes, and thus to the image points $\tilde{p}_{\mathrm{L}}$ and $\tilde{p}_{\mathrm{R}}$ motions. So, we obtain

$${}^{0}\dot{\underline{\mathbf{n}}} \times (\mathbf{h}_{\mathrm{R}} \times \mathbf{h}_{\mathrm{L}}) + {}^{0}\underline{\mathbf{n}} \times \left(\dot{\mathbf{h}}_{\mathrm{R}} \times \mathbf{h}_{\mathrm{L}}\right) + {}^{0}\underline{\mathbf{n}} \times \left(\mathbf{h}_{\mathrm{R}} \times \dot{\mathbf{h}}_{\mathrm{L}}\right) = 0 \tag{14}$$

By considering that $\dot{\mathbf{h}}_{\mathrm{L}} = {}^{0}\mathbf{F}_{\mathrm{L}}\,\dot{\tilde{p}}_{\mathrm{L}}$ and $\dot{\mathbf{h}}_{\mathrm{R}} = {}^{0}\mathbf{F}_{\mathrm{L}}\,\dot{\tilde{p}}_{\mathrm{R}}$ and with some reorganizations (details can be found in [19]), equation (14) can be rewritten as follows

$${}^{0}\dot{\underline{\mathbf{n}}} \times (\mathbf{h}_{\mathrm{R}} \times \mathbf{h}_{\mathrm{L}}) = -{}^{0}\underline{\mathbf{n}} \times \left(\left({}^{0}\mathbf{F}_{\mathrm{R}}\,\dot{\tilde{p}}_{\mathrm{R}}\right) \times \mathbf{h}_{\mathrm{L}}\right) - {}^{0}\underline{\mathbf{n}} \times \left(\mathbf{h}_{\mathrm{R}} \times \left({}^{0}\mathbf{F}_{\mathrm{L}}\,\dot{\tilde{p}}_{\mathrm{L}}\right)\right) \tag{15}$$

Now, it is necessary to relate the laser beam angular velocity ${}^{0}\dot{\underline{\mathbf{n}}}$ to the mirror rotational velocity (pan-tilt angular rotations). Let us consider Ω [1] the laser beam angular velocity. So, the time-derivation of ${}^{0}\underline{\mathbf{n}}$ can be written as follows

$${}^{0}\dot{\underline{\mathbf{n}}} = \Omega \times {}^{0}\underline{\mathbf{n}} \implies \Omega = {}^{0}\underline{\mathbf{n}} \times {}^{0}\dot{\underline{\mathbf{n}}} \tag{16}$$

Thereby, by identifying equations (15) and (16), we can easily deduce (after some mathematical arrangements) the expression of the mirror velocity as a function of the laser spot velocities in the image planes

$$\Omega = -\frac{\mathbf{h}_{\mathrm{R}} \times \mathbf{h}_{\mathrm{L}}}{\|\mathbf{h}_{\mathrm{R}} \times \mathbf{h}_{\mathrm{L}}\|^2} \times \left(\mathbf{h}_{\mathrm{L}} \times \left({}^{0}\mathbf{F}_{\mathrm{R}}\,\dot{\tilde{p}}_{\mathrm{R}}\right) - \mathbf{h}_{\mathrm{R}} \times \left({}^{0}\mathbf{F}_{\mathrm{L}}\,\dot{\tilde{p}}_{\mathrm{L}}\right)\right) \tag{17}$$

Remark 2: *It can be highlighted that (17) allows computing directly the angular velocity Ω of the actuated mirror using the pseudo-control inputs $\dot{\tilde{p}}_{\mathrm{R}}$ and $\dot{\tilde{p}}_{\mathrm{L}}$ without any matrices inversion (even less tensors manipulation and inversion) or numerical approximation.*

III. 3D PATH FOLLOWING USING THREE-VIEW GEOMETRY

At this stage, we have all of the *"ingredients"* to implement a three-view based 3D path following control law able to operate on any 3D scene without any prior knowledge or 3D reconstruction of the scene and without additional sensors. To the best of our knowledge, this kind of approach has never been treated in the literature.

So, let us present the design of the complete 3D path following control law for laser steering.

---

[1] Note that Ω is the mirror angular velocity whereas ω is that of the laser spot in the image frame $\mathcal{R}_0$.

A. Design of the 3D Control Law

In the previous section, we have shown that thanks to the trifocal constraint, it is possible to link the angular velocity of an actuated mirror (or the laser beam velocity), to those of the laser spot $\dot{\tilde{p}}_L$ and $\dot{\tilde{p}}_R$ defined in both the left and right images frames $\mathcal{R}_i$ ($i \in [L,R]$). Therefore, the problem of 3D path following can be seen as the combination of two coherent 2D path following controllers, initially expressed separately in the images frames, thanks to the trifocal constraint.

Recall that the laser spot velocity $\mathbf{v}_L$ (respectively, $\mathbf{v}_R$), in the *Frénet* frame $\mathcal{R}_s$ (attached to the curve to be tracked), is obtained using (7).

$$\mathbf{v}_L = \frac{\dot{\tilde{p}}_L + \omega \times \dot{\tilde{p}}_L}{\left\| \dot{\tilde{p}}_L + \omega \times \dot{\tilde{p}}_L \right\|}, \quad \text{and} \quad \mathbf{v}_R = \frac{\dot{\tilde{p}}_R + \omega \times \dot{\tilde{p}}_R}{\left\| \dot{\tilde{p}}_R + \omega \times \dot{\tilde{p}}_R \right\|} \quad (18)$$

where $\dot{\tilde{p}}_L$ and $\dot{\tilde{p}}_R$ are obtained by the numerical differentiation of $\tilde{p}_L$ and $\tilde{p}_R$, respectively (computed thanks to the dot visual tracking algorithm).

Thereby, by putting the expressions of $\mathbf{v}_L$ and $\mathbf{v}_R$ (18) in (17), we obtain the angular velocity of the mirror as a function of the 2D coherent velocities $\mathbf{v}_L$ and $\mathbf{v}_R$, then function of $\dot{\tilde{p}}_L$ and $\dot{\tilde{p}}_R$. So, at each iteration, it becomes possible to compute the new angular velocity using the following equation

$$\Omega = -\eta \times \left(\mathbf{h}_L \times (^0\mathbf{F}_R \mathbf{v}_R) - \mathbf{h}_R \times (^0\mathbf{F}_L \mathbf{v}_L) \right) \quad (19)$$

then,

$$\Omega = -\eta \times \left(\mathbf{h}_L \times \left(^0\mathbf{F}_R \frac{\dot{\tilde{p}}_R + \omega \times \dot{\tilde{p}}_R}{\left\| \dot{\tilde{p}}_R + \omega \times \dot{\tilde{p}}_R \right\|} \right) \right.$$
$$\left. - \mathbf{h}_R \times \left(^0\mathbf{F}_L \frac{\dot{\tilde{p}}_L + \omega \times \dot{\tilde{p}}_L}{\left\| \dot{\tilde{p}}_L + \omega \times \dot{\tilde{p}}_L \right\|} \right) \right) \quad (20)$$

where $\eta = \frac{\mathbf{h}_R \times \mathbf{h}_L}{\|\mathbf{h}_R \times \mathbf{h}_L\|^2}$ which has the same effect as control gain.

Note that the expression of the angular velocity Ω, containing the 3D geometry proprieties of the observed scene, is obtained (thanks to the revisited trifocal constraint formulation) without any 3D reconstruction or prior knowledge on the observed scene.

Now, it is necessary to convert Ω into the mirror joint velocities $\dot{q}_1$ and $\dot{q}_2$ using the inverse differential kinematic matrix (IDKM) $\mathbf{D}^{-1}$ of the pan-tilt mirror as $\dot{\mathbf{q}}_i = \mathbf{D}^{-1}\Omega$. As it has been claimed, our controller must be robust to the different calibration errors (camera, robot, and Eye-Hand calibrations), thus $\mathbf{D}^{-1}$ is chosen equal to $\begin{pmatrix} 1 & 0 \\ 0 & 1 \end{pmatrix}$.

IV. SIMULATION VALIDATION

Before implementing the proposed control law on an experimental work-flow; it has been validated using a MATLAB-based simulator. In order to be as close as possible to the experimental conditions, the developed simulator includes the mains components implemented in the experimental set-up. Therefore, two cameras (a stereoscopic vision system), a laser source, an actuated mirror and a 3D object are reproduced in the simulator (Fig. 6). Also, the different components are positioned in aim to mimic the real configuration of laser surgical system (e.g., the endoscopic tip studied in [25]). Also, the validation tests were performed under favourable and unfavourable working conditions (measurement errors, calibration errors, deformable targets, etc.) in order to access the control law performance and behavior (accuracy, robustness and repeatability).
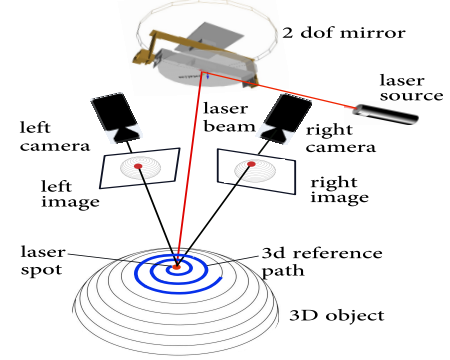
Fig. 6. Overview of the developed simulator.

A. Initialization

1) Calibration parameters: as demonstrated in the following, the proposed control law requires only weak calibrations (camera and Euclidean Hand-Eye calibrations). This includes the camera intrinsic parameter matrix ($\mathbf{K}_L$ and $\mathbf{K}_R$) of each camera as well as the pose of the mirror with respect to each camera frame. Due the fact that the *actuated mirror is considered as a virtual camera which grabs one pixel at a time*, it is possible to compute the fundamental matrices $^0\mathbf{F}_L$ and $^0\mathbf{F}_R$ ((10), (11)) between the mirror and both the left and right cameras, respectively. The simulator presented here was built using the following matrices:

- $\mathbf{K}_L = \mathbf{K}_R = \begin{pmatrix} 900 & 0 & 320 \\ 0 & 900 & 240 \\ 0 & 0 & 1 \end{pmatrix}$, the cameras' intrinsic parameters matrices;
- $^0\mathbf{F}_L = [^0\mathbf{t}_L]_\wedge\, ^0\mathbf{R}_L \mathbf{K}^{-1}$, the fundamental matrix, between the virtual view and the left camera, is obtained (rough estimation) by a translation vector $^0\mathbf{t}_L$ = (-40, 35, -20)$^\top$ (mm) and a rotation matrix $^0\mathbf{R}_L = \mathbf{I}_{3\times3}$;
- Similarly, $^0\mathbf{F}_R = [^0\mathbf{t}_R]_\wedge\, ^0\mathbf{R}_R \mathbf{K}^{-1}$ is obtained (also a rough estimation) by a translation vector $^0\mathbf{t}_L$ = (40, 35, -20)$^\top$ (mm) and a rotation matrix $^0\mathbf{R}_R = \mathbf{I}_{3\times3}$.

The simulated cameras have a resolution of 640×480 pixels, a principal point coordinates (u_0, v_0) = (320, 240) pixels, a focal length $f_x = f_y = 900$ pixels, and an acquisition rate of 25 frames per second. The actuated mirror is placed at a distance D = 20 mm to the center of the 3D object (here a portion of a sphere).

Remark 3: *the only accurate calibration which is needed is the fundamental matrix $^R\mathbf{F}_L$ between the left and the right image. It allows retrieving a coherent Γ_R using the curve defined by the operator within the left image. The matrix $^R\mathbf{F}_L$ is independent from the control law functioning. It is computed one off-line and only once.*

2) Controller gains tuning: here, we have studied the impact of the control gains α_1 and α_2 on the 3D path following accuracy (using the root mean square (RMS) error between the reference and the performed paths) in order to find their optimal values. Hence, we varied α_1 and α_2 from 0.1 to 0.6 (with a step of 0.1) and the obtained results are reported in Table I. As can be highlighted, the optimal pair of gains for which we get the best accuracy (0.041 mm) are $\alpha_1 = 0.4$ and $\alpha_2 = 0.3$. These gains are used for the whole simulation scenarios described below.

TABLE I
IMPACT OF THE GAINS α_1 AND α_2 ON THE 3D PATH FOLLOWING
ACCURACY [$\times$ = TEST FAILED].

		α_2					
		0.1	0.2	**0.3**	0.4	0.5	0.6
	0.1	$\times$	0.0921	0.1573	0.2364	0.3150	0.3965
	0.2	$\times$	0.0800	0.0772	0.1155	0.1539	0.1948
	0.3	1.9311	0.0574	0.0525	0.0745	0.1025	0.1265
α_1	**0.4**	$\times$	$\times$	**0.0410**	0.0560	0.0745	0.0929
	0.5	$\times$	1.3236	0.0506	0.1039	0.0588	0.0746
	0.6	$\times$	$\times$	0.1963	$\times$	0.0526	1.1056

B. Validation with a Static Object

1) Without external disturbances: firstly, the proposed controller was validated onto 3D static objects without any external disturbances (e.g., deformations). This means that Γ_L and Γ_R are time-invariant. The 3D object chosen to illustrate the functioning of the controller consists of a sphere viewed by both left and right cameras.

Let us consider a portion of the viewed sphere **S** *measuring: diameter= 30 mm and height= 10 mm* in which a 3D curve Γ_{3d} (*spherical helix*) is defined with respect to the world frame $\mathcal{R}_w$. Thereby, the 3D curve is projected in the image plane using the projection matrices $^w\mathbf{P}_i$ defined by

$$^w\mathbf{P}_L = \mathbf{K}_L \left[\mathbf{I/0}\right] \mathbf{M}_L \tag{21}$$

where

$$\mathbf{M}_L = \begin{bmatrix} {}^0\mathbf{R}_L & {}^0\mathbf{t}_L \\ 0 & 1 \end{bmatrix} \tag{22}$$

The error between the reference and the performed path are denoted by e_L and e_R (in both mm and pixels) computed respectively by

$$e_L = \begin{pmatrix} \tilde{p}_L(x) - a_L(x) \\ \tilde{p}_L(y) - a_L(y) \end{pmatrix}, \quad \text{and} \quad e_R = \begin{pmatrix} \tilde{p}_R(x) - a_R(x) \\ \tilde{p}_R(y) - a_R(y) \end{pmatrix},$$

while the error in the global frame $\mathcal{R}_w$ is refereed by e_w (mm).

In Fig. 7, some snapshots are depicted (iterations $i = [1, 200, 350]$) acquired during the 3D path following process using an initial velocity of $\mathbf{v}_0 = 25$ mm/seconds.
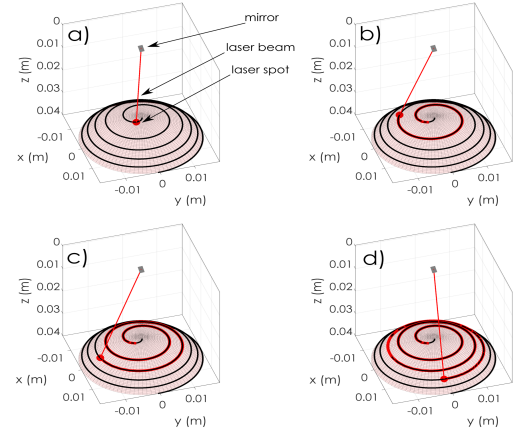
Fig. 7. Some snapshots acquired during the 3D path following: (a) initial (at the iteration $i = 0$), (b)-(c) intermediates, and (d) final positions of the laser spot (please see Multimedia Extension 1).

Namely, Fig. 7(a) depicts the initial position of the laser spot Fig. 7(b),(c) intermediate positions and Fig. 7(d) the 3D path following achievement. In the same, both the reference and the followed 3D paths are projected in $\mathbf{I}_L$ and $\mathbf{I}_R$ (Fig. 8). It can be highlighted that the path following controller demonstrates a perfect superposition of both paths (reference + performed) meaning the high accuracy of the proposed method.
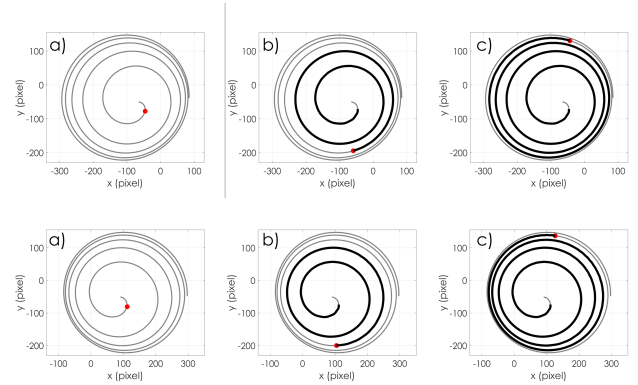
Fig. 8. Superposition of the reference and performed paths in $\mathbf{I}_L$ (first line) and $\mathbf{I}_R$ (second line)
.

Also, the evolution of the error during the path following was computed at each iteration i. So, Fig. 9(a),(b) represents the error e_L in the left image, and e_R in the right image, respectively. It can be underlined that both errors e_L and e_R are very low, also similar, demonstrating the good accuracy of the proposed control law. Similarly, the error e_w, expressed in the global frame $\mathcal{R}_w$, is still very low (Fig. 9(c)). More precisely, the RMS error of e_L is 0.023 mm (equivalent to 0.25 pixel), e_R is 0.022 mm (equivalent to 0.24 pixel), and e_w is 0.033 mm.

2) Various initial velocities $\mathbf{v}_0$: in order to show the control law accuracy depending on initial laser spot velocity $\mathbf{v}_0$, we repeat the path following task several times by increasing
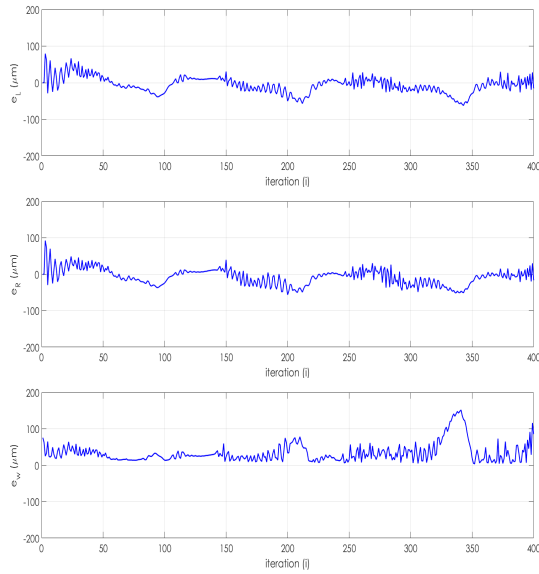
Fig. 9. [Static object]: path following errors: (first line) is e_{L}, (second line) is e_{R}, and (third line) is e_{w}.

$\mathbf{v}_0$ from 15 to 32 mm/second. As shown in Table II, despite the velocity increase (more than the double of the initial value), the path following errors remain very stable.

TABLE II

ACCURACY ANALYSIS ON A SPHERICAL HELIX CURVE [$\mathbf{v}_0$ (MM/SECOND), $e_{\mathrm{L/R}}$ (MM), e_{w} (MM)].

$\mathbf{v}_0$	RMS (e_{L})	RMS (e_{R})	RMS (e_{w})
15	0.027	0.030	0.038
16	0.033	0.029	0.037
21	0.026	0.026	0.035
25	0.023	0.022	0.033
30	0.026	0.026	0.036
32	0.034	0.027	0.039

Furthermore, we have also experimented the performances of the proposed control law using different initial velocity $\mathbf{v}_0$. The objective is to demonstrate that the velocity profile is completely independent from initial velocity, time as well as curve shape. Indeed, by analysing Fig. 10, one can remark that despite the different initial velocity values, the profile of the forward laser spot velocity remains "almost" the same among the different scenarios. However, the curves are not superimposed since the controller performs the same path in less iterations when the speed is higher and *vice-versa*.

3) With measurement errors: the same validation tests were reproduced by adding an uniform noise on the laser spot detection (similar to measurement error in real conditions). For instance, for a reference velocity $\mathbf{v}_0 = 25$ mm/second, we add a noise that range from 1% to 40% of the measured laser spot position. Again, we have computed the different errors e_{L}, e_{R}, and e_{w} for each noise value as reported in Table III.

C. Validation with a Deformable Object

Now, we will focus on the ability of our method to operate on deformable 3D scenes (similar to an object in motion, or
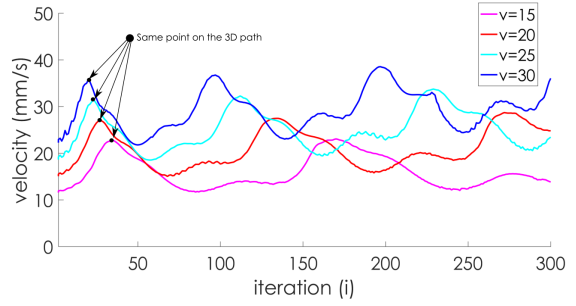
Fig. 10. Velocity profiles of the laser spot forward.

TABLE III

ACCURACY ANALYSIS OF CONTROLLER BY ADDING NOISE ON THE LASER SPOT DETECTION [$\mathbf{v}_0$ (MM/SECOND), NOISE (%), $e_{\mathrm{L/R}}$ (MM) AND e_{w} (MM)].

velocity	noise	RMS (e_{L})	RMS (e_{R})	RMS (e_{w})
	1	0.023	0.023	0.031
	10	0.045	0.045	0.053
$\mathbf{v}_0 = 25$	20	0.062	0.061	0.099
	30	0.101	0.099	0.169
	40	0.112	0.109	0.184

an anatomic organ under breathing and/or heartbeat effects, etc.). This means that the curve $\Gamma_{3d}(t)$ is time-varying i.e., its size and position change over time.

Let us consider again a spherical helix curve by adding a sinusoidal deformation on it (the sphere volume increases and decreases of $\pm800\%$ during the path following task). This means that the height of the sphere varies from 10mm to 40mm (with a speed of 6mm/second), when its diameter changes from 30mm to 120mm (with a speed of 18mm/second) (please see Multimedia Extension 1).
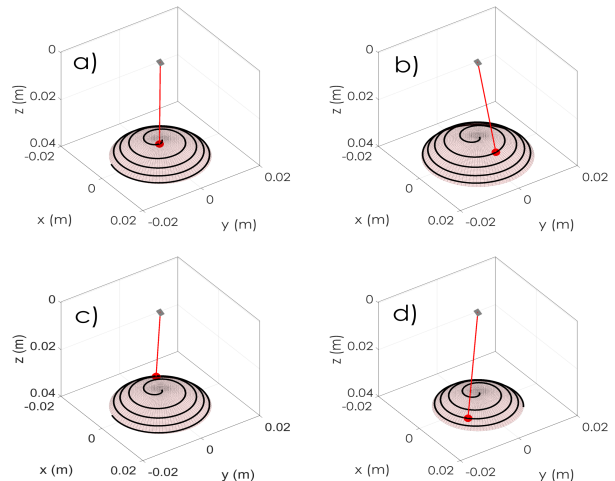
Fig. 11. Some images acquired during the 3D path following achieved using a 3D dynamic curve $\Gamma_{3d}(t)$ (please see Multimedia Extension 1).

Fig. 11 shows some snapshots (captured at iterations $i = [1, 50, 150, 300]$) illustrating the 3D path following achievement under large deformations of $\Gamma_{3d}(t)$. It can be underlined that despite important changes of the curve size, the control law remains robust. Furthermore, be observed in Fig. 12 that the following errors (both in image and world frames) remain very low (lower than 0.1 mm).
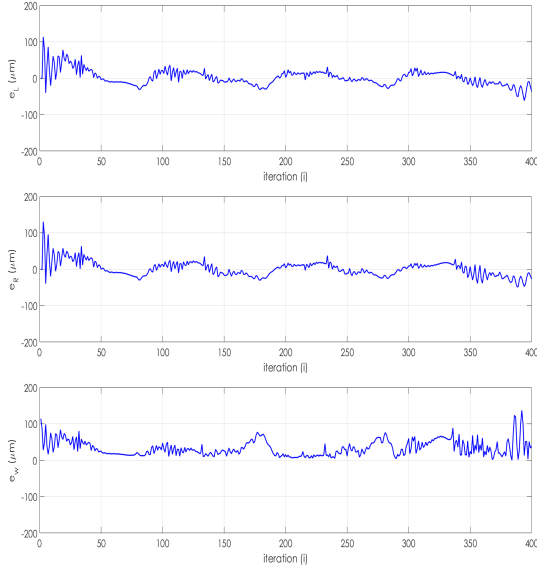
Fig. 12. [Deformable object]: path following errors: (first line) is e_L, (second line) is e_R, and (third line) is e_w.

This task is repeated several times in order to judge the controller efficiency with a dynamic curve and different initial laser spot velocity $\mathbf{v}_0$. Indeed, Table IV summarizes the obtained numerical values. As can be noticed the image error e_L varies from 0.029 mm to 0.045 mm (similarly, e_R changes from 0.030 mm to 0.046 mm) when the velocity input changes from the simple to the double (i.e., from 15 to 32 mm/second). By a qualitative comparison based on Table II (static scene), one can note that the accuracy remains similar in both static and dynamic scenes. The same conclusion can be made about the error e_w expressed in the global frame.

TABLE IV
ACCURACY ANALYSIS ON A DEFORMABLE SCENE [$\mathbf{v}_0$ (MM/SECOND),
$e_{L/R}$ (MM), e_w (MM)].

$\mathbf{v}_0$	RMS (e_L)	RMS (e_R)	RMS (e_w)
15	0.029	0.030	0.045
16	0.025	0.026	0.041
21	0.021	0.021	0.035
25	0.025	0.021	0.040
30	0.053	0.048	0.057
32	0.045	0.046	0.050

V. EXPERIMENTAL VALIDATION

This section presents a series of experiments allowing to analyze the performance of the algorithm in real conditions.

The object representing the target is a potato chip (crisp). With respect to the shapes of the laser path, the tests were performed both on programmed paths (basic geometric shapes) and manually defined paths.

A. Experimental Set-up
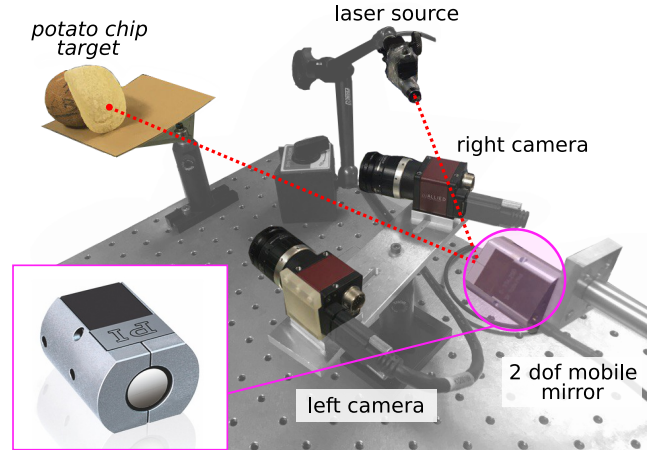
Fig. 13. Photography of the experimental set-up.

The developed approach was experimentally validated using the set-up depicted in Fig. 13. It consists of two CCD cameras (frame rate of 25 images per second grabbing images of resolution of 640×480 pixels), a laser source (laser pointer), an 2 DoF actuated mirror (the S-334 from Physical Instruments (PI) Inc[2]). The PI mirror has a parallel-architecture based in three coplanar axes and a fixed pivot point. Consequently, the mirror provides two rotations (α and β) with a large bandwidth (1kHz), a resolution of 0.2 μrad, a linearity of 0.05 %, and a motion range of $[-0.026\ rad, +0.026\ rad]$.

As can be shown in Fig. 13, both the CCD cameras and the actuated mirror are mounted in order to reproduce a three-view geometry configuration, similarly to simulator presented in Section IV

B. Definition of Γ_L and Γ_R in an Experimental Conditions

As mentioned in Section II, the paths to be followed consist of a non-parametrized curves (i.e., parametric equation is not available) Γ_L and Γ_R. This means that each curve contains a set of 2D points independently of time t. For instance, to define the curves, first, the operator, using a tactile tablet and a stylus, draws a 2D curve Γ_L in the left image $\mathbf{I}_L$ [26]. Second, to obtain the corresponding curve Γ_R, in $\mathbf{I}_R$, one can use an accurate matching between $\mathbf{I}_L$ and $\mathbf{I}_R$ based on the epipolar geometry proprieties. To do that, we start by computing the fundamental matrix $^L\mathbf{F}_R$ using a robust estimation technique such as random-sample consensus (RANSAC) algorithm [24]. Note that this matrix is computed only once (off-line) and should not change over time (both left and right cameras are rigidly attached).

[2]http://www.physical-instruments.fr

Indeed, the fundamental matrix ${}^{\mathrm{L}}\mathbf{F}_{\mathrm{R}}$ can be estimated using a high textured scene (calibration template), if it is necessary.
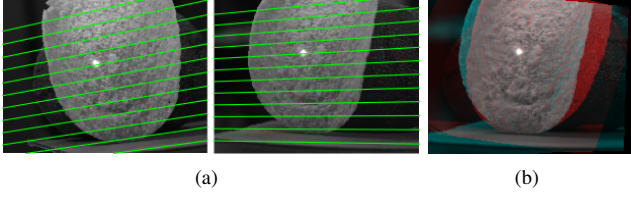
Fig. 14.   a) computed epipolar lines in left image $\mathbf{I}_{\mathrm{L}}$ in right image $\mathbf{I}_{\mathrm{R}}$ before rectification. b) rectificied images in the form of stereo anaglyph.

Thereby, using the fundamental matrix, it is possible to rectify both images (Fig. 14) by their projections in the same image plane in such a way that the corresponding points have the same row coordinates. This image projection makes the images appear as though the image planes of both cameras are coplanar. Also, this means that all the epipolar lines, in both images, are horizontal and parallel.

Let us consider that the a_i $(i = 1, \cdots, N)$ are the set of 2D points defining Γ_{L}). Therefore, to retrieve the corresponding curve Γ_{R} in $\mathbf{I}_{\mathrm{R}}$, we use a zero-mean normalized cross correlation algorithm (well-known points matching method in stereovision). Therefore, for each point $a_{i\mathrm{L}}$, in the rectified image $\mathbf{I}_{\mathrm{Lc}}$, we search the corresponding point $a_{i\mathrm{R}}$ in the right rectified image $\mathbf{I}_{\mathrm{Rc}}$ through the corresponding horizontal epipolar line to which the point belongs (Fig. 15(a)). Consequently, we obtain two coherent 2D curves representing the path to be followed in each image as can be shown in Fig. 15(b) (please see Multimedia Extension 1).
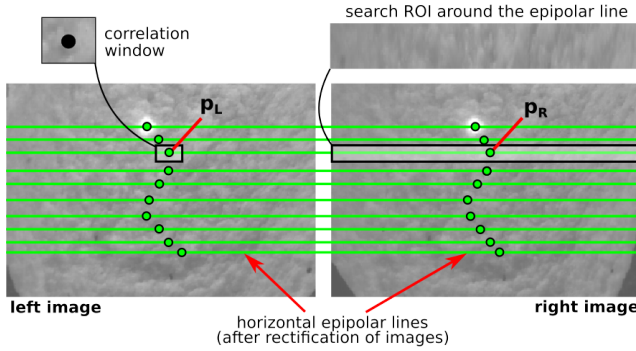
Fig. 15.   Example showing the definition of two coherent curves in stereo-images. (a) a set of 2D points (Γ_{L}) defined by an operator, in $\mathbf{I}_{\mathrm{Lc}}$, and (b) the corresponding 2D points (Γ_{R}) in $\mathbf{I}_{\mathrm{Rc}}$ computed automatically using the epipolar geometry proprieties (please see Multimedia Extension 1).

Now, it is possible to compute the velocity of the laser spot $\mathbf{v}_{\mathrm{L}}$ and $\mathbf{v}_{\mathrm{R}}$ in each image $\mathbf{I}_{\mathrm{L}}$ and $\mathbf{I}_{\mathrm{R}}$, respectively. These velocities will be "injected" into the global control law expressed in (20).

To follow the different steps of the proposed controller, one can refer to the *Algorithm 1* which summarizes the mains stages of the proposed method.

Algorithm 1: Main steps of the control law.

> initialize $(\mathbf{v}_0, \alpha_1, \alpha_2)$
> get cameras intrinsic parameters $\mathbf{K}_{\mathrm{L}}, \mathbf{K}_{\mathrm{R}}$
> estimate roughly ${}^{0}\mathbf{F}_{\mathrm{R}}, {}^{0}\mathbf{F}_{\mathrm{L}}$
> estimate accurately ${}^{\mathrm{L}}\mathbf{F}_{\mathrm{R}}$
> rectify $\mathbf{I}_{\mathrm{R}}$ and $\mathbf{I}_{\mathrm{L}}$
> define Γ_{L} using $\mathbf{I}_{\mathrm{L}}$
> define automatically Γ_{R} using ${}^{\mathrm{L}}\mathbf{F}_{\mathrm{R}}$
> **begin**
> > grab image $\mathbf{I}_{\mathrm{L}}$
> > grab image $\mathbf{I}_{\mathrm{R}}$
> > detect laser spot position $\tilde{p}_{\mathrm{L}}$ in $\mathbf{I}_{\mathrm{L}}$
> > detect laser spot position $\tilde{p}_{\mathrm{R}}$ in $\mathbf{I}_{\mathrm{R}}$
> > compute $\mathbf{v}_{\mathrm{L}} \longleftarrow (\dot{\tilde{p}}_{\mathrm{L}}, \omega)$
> > compute $\mathbf{v}_{\mathrm{R}} \longleftarrow (\dot{\tilde{p}}_{\mathrm{R}}, \omega)$
> > compute Ω and ${}^{0}\underline{\dot{\mathbf{n}}} \longleftarrow (\tilde{p}_{\mathrm{L}}, \tilde{p}_{\mathrm{R}}, \mathbf{v}_{\mathrm{L}}, \mathbf{v}_{\mathrm{R}}, {}^{0}\mathbf{F}_{\mathrm{L}}, {}^{0}\mathbf{F}_{\mathrm{R}})$
> > convert Ω to $\dot{\mathbf{q}}_1, \dot{\mathbf{q}}_2 \longleftarrow (\Omega, \mathbf{D})$

C. Control Loop Initialization

1) Calibration parameters: As it was already mentioned, the proposed control law does not require accurate calibration of neither camera parameters nor relative poses between the cameras and the mirror. Therefore, for the experimental setup presented previously, all of the parameters (except for the fundamental matrix between two views) were measured using a ruler, literally.

First, we start with the estimation of intrinsic parameters of both cameras. As the cameras used are equipped with the same objective lenses, the matrices of intrinsic parameters were considered to be equal. So,

$$\mathbf{K}_{\mathrm{L}} = \mathbf{K}_{\mathrm{R}} = \begin{pmatrix} 2811 & 0 & 320 \\ 0 & 2811 & 240 \\ 0 & 0 & 1 \end{pmatrix}$$

As the focal length ($f = 2811$) expresses the ration $\frac{pixel}{m}$, its value was measured simply by comparing the real size of the object (about 4.5 cm) with its size on the image expressed in pixels and considering the camera-object distance which was approximately equal to 27.5 cm.

Next step consists of the estimation of the fundamental matrices between the cameras and the virtual image (${}^{0}\mathbf{F}_{\mathrm{L}}$ and ${}^{0}\mathbf{F}_{\mathrm{R}}$). Both these matrices depend on the relative disposition between the cameras and the mirror, each one characterized by a translation and a rotation:

$$\begin{aligned} {}^{0}\mathbf{t}_{\mathrm{L}} &= (0.030, 0.040, -0.110)^{\top} \\ {}^{0}\mathbf{t}_{\mathrm{R}} &= (0.030, -0.055, -0.105)^{\top} \\ {}^{0}\mathbf{R}_{\mathrm{L}} &= \mathbf{R}_{\mathrm{z}}(-15°)\mathbf{R}_{\mathrm{x}}(170°) \\ {}^{0}\mathbf{R}_{\mathrm{R}} &= \mathbf{R}_{\mathrm{x}}(190°) \end{aligned}$$

Finally, we obtain the final expressions for fundamental matrices as follows: ${}^{0}\mathbf{F}_{\mathrm{L}} = [{}^{0}\mathbf{t}_{\mathrm{L}}]_{\wedge} {}^{0}\mathbf{R}_{\mathrm{L}} \mathbf{K}^{-1}$ and ${}^{0}\mathbf{F}_{\mathrm{R}} = [{}^{0}\mathbf{t}_{\mathrm{R}}]_{\wedge} {}^{0}\mathbf{R}_{\mathrm{R}} \mathbf{K}^{-1}$.

2) Controller gains tuning: at this step, it is important to point out the difference between the real setup and simulation. In fact, in real setup the distance from mirror to object is much higher (about 40 cm) which explains the fact that the same values of gains cannot be used. Experimentally, the following set was determined as optimal: $\alpha_1 = 0.08$, $\alpha_2 = 0.6$.

D. Experiments

As it was mentioned above, the algorithm was tested on five paths with different shapes displayed on Fig. 16. The results are represented in Table V. The mean error of laser spot positioning on the path is of the order of 2 pixel which corresponds to a value lower than one millimeter. It is important to note that the mirror is located 40 cm away, therefore, the error may be lowered by positioning the target closer to laser source. However, it is not possible for some applications that impose constraints on the laser-target distance, such as surgical operations.
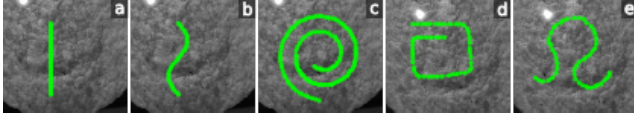
Fig. 16. Different paths realized: (a) line, (b) sine, (c) spiral, (d) sigma, (e) leo. Paths (a)-(c) were programmed, while the points for paths (d) and (e) were defined manually (please see Multimedia Extension 1).

Remark that all paths performed within the framework of this study have very different curvature: from line (no curvature at all), sine (low curvature) to a spiral or manually defined paths containing curved edges: the laser should completely change the direction within several points on the curve. Nonetheless, as can be seen from Table V, the standard deviation and RMS stay both inferior to one millimeter which proves the robustness of the algorithm towards variable path curvature. The last point we want to mention is that

TABLE V
ACCURACY ANALYSIS OF SEVERAL 3D PATHS.

	$e_{\mathrm{L/R}}$ (px)			$e_{\mathrm{L/R}}$ (mm)		
	MEAN	STD	RMS	MEAN	STD	RMS
line	2.45	1.12	2.70	0.87	0.39	0.96
sine	2.23	1.29	2.58	0.79	0.46	0.91
spiral	2.80	1.96	3.44	0.99	0.69	1.22
sigma	2.35	1.37	2.72	0.83	0.48	0.97
leo	2.02	1.48	2.51	0.72	0.52	0.89

the method was tested both on programmed and manually defined paths. Programmed paths were obtained simply as a set of points on a standard mathematical function (line, sine, spiral). Obviously, in many cases, it is not enough. Therefore, we tested the method on a manually defined paths where the points were acquired with mouse clicks on the left image. In both cases, the paths were than transfered from left to right image using the procedure presented in Section V-C. As a result, the algorithm shows very good results on both types of paths.
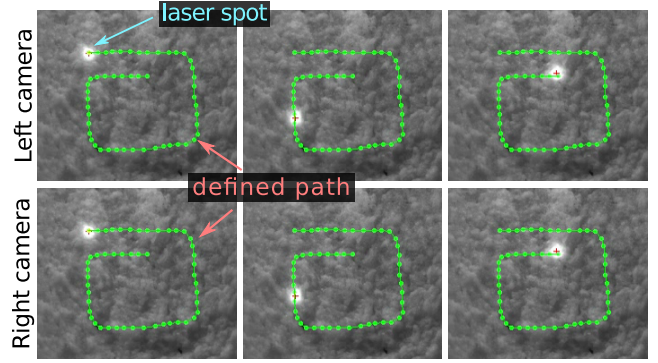
Fig. 17. Some images acquired during the 3D path following, *sigma* path (please see Multimedia Extension 1)
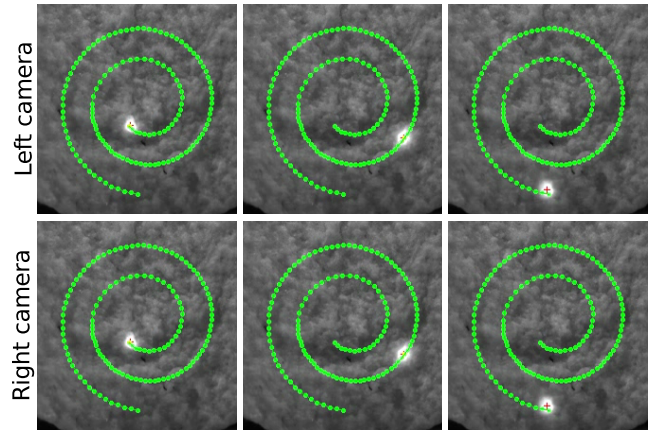
Fig. 18. Some images acquired during the 3D path following, *spiral* path (please see Multimedia Extension 1)

VI. CONCLUSION

In this paper, a vision-based controller for 3D laser steering was presented. It consisted of the association of the advantages of a path following scheme with those of a three-view geometry system into the same control law. The developed approach is able to work in both 2D and 3D paths without any prior knowledge on the scene.

The proposed method was successfully validated both in simulation and experimentally. Several validation scenarios were implemented, e.g., static and deformable objects as well as favourable and unfavourable working conditions. In all cases, the laser steering control law showed its ability to operate accurately even with poor calibration parameters.

The next stage will consist of the implementation of the controller on a laser surgery endoscopic system that is currently under development.

REFERENCES

[1] T. Sibillano, A. Ancona, V. Berardi, and P. Lugarà, "A real-time spectroscopic sensor for monitoring laser welding processes," *Sensors*, vol. 9, pp. 3376–3385, 2009.
[2] B. Petrak, K. Konthasinghe, S. Perez, and A. Muller, "Feedback-controlled laser fabrication of micromirror substrates," *Rev. of Scient. Inst.*, vol. 82, pp. 112–123, 2011.
[3] B. Aronoff, "Lasers in general surgery," *World J. of Surgery*, vol. 7, no. 6, pp. 681–683, 1983.

[4] H. Yamanaka, K. Masamune, T. Chiba, and T. Dohi, "An endoscope with 2 DOFs steering of coaxial nd:yag laser beam for fetal surgery," *IEEE/ASME T. on Mech.*, vol. 15(6), pp. 898–905, 2010.

[5] E.-J. Jung, J.-H. Lee, B.-J. Yi, J. Park, S. Yuta, and S.-T. Noh, "Development of a laser-range-finder-based human tracking and control algorithm for a marathoner service robot," *IEEE/ASME T. on Mech.*, vol. 19, no. 6, pp. 1963–1976, 2014.

[6] J. H. Park, H. S. Lee, S. O. Yun, Y. B. Ham, D. W. Yun, "Design of a piezoelectric-driven tilt mirror for a fast laser scanner," *Japanese J. of Applied Phys.*, vol. 51, 2012.

[7] L. W. Huikai Xie, Jingjing Sun, "Optical micro-endoscope for 3d in-vivo imaging," *SPIE Biom. Optics and Med. Imag.*, 2012.

[8] R. Renevier, B. Tamadazte, K. Rabenorosoa, and N. Andreff, "Endoscopic Laser Surgery: Design, Modeling, and Control," *IEEE T. on Mech.*, 22(1), pp. 99–106, 2017.

[9] Y. Huang, Y. Xiao, P. Wang, and M. Li, "A seam-tracking laser welding platform with 3d and 2d visual information fusion vision sensor system," *Int. J. of Adv. Manuf. Tech.*, 67, pp. 415–426, 2012.

[10] N. Tsuchiya, S. Gibson, T. C. Tsao and M. Verhaegen, "Receding-Horizon Adaptive Control of Laser Beam Jitter," in IEEE/ASME T. on Mech., vol. 21(1), pp. 227-237, 2016.

[11] J.-A. Seon, B. Tamadazte, and N. Andreff, "Decoupling path following and velocity profile in vision-guided laser steering," *IEEE T. on Rob.*, vol. 31(2), pp. 280–289, 2015.

[12] B. Tamadazte and N. Andreff, "Weakly calibrated stereoscopic visual servoing for laser steering: Application to phonomicrosurgery," in *IEEE/RSJ Int. Conf. on Intel. Rob. and Syst.*, 2014, pp. 743–748.

[13] M. Bosse and R. Zlot, "Continuous 3d scan-matching with a spinning 2d laser," in *IEEE Int. Conf. on Rob. and Auto.*, 2009, pp. 4312–4319.

[14] S. Alajlouni, "Solution to the Control Problem of Laser Path Tracking Using Risley Prisms," *IEEE T. on Mech.*, 21(4), pp. 1892 - 1899, 2016.

[15] M. Fridenfalk and G. Bolmsjo, "Design and validation of a universal 6D seam-tracking system in robotic welding using arc sensing," *Adv. Rob.*, vol. 18, pp. 1–21, 2004.

[16] T. L. Bui, P. T. Doan, S. S. Park, H. K. Kim, S. B. Kim "AGV trajectory control based on laser sensor navigation," *Int. J. of Sci. and Eng.*, vol. 4, pp. 16–20, 2013.

[17] A. Aguiar and J. Hespanha, "Trajectory-tracking and path-following of underactuated autonomous vehicles with parametric modeling uncertainty," *IEEE T. on Auto. Cont.*, vol. 52(8), pp. 1362–1379, 2007.

[18] P. Morin and C. Samson, "Motion control of wheeled mobile robots," in *Springer Handbook of Rob.*, B. Siciliano and O. Khatib, Eds. Springer Berlin Heidelberg, 2008, pp. 799–826.

[19] N. Andreff and B. Tamadazte, "Laser steering using virtual trifocal visual servoing," *Int. J. of Rob. Res.*, *in press*, 2015.

[20] R. W. Brockett, "Asymptotic stability and feedback stabilization," in *Differential Geometric Control Theory*, Boston, 1983, pp. 181–191.

[21] R. Hartley and A. Zisserman, *Multiple view geometry in computer vision*, 2nd ed, Cambridge University Press, 2006.

[22] D. Sabatta and R. Siegwart, Vision-based path following using the 1D trifocal tensor, in *IEEE Int. Conf. on Rob. and Auto.*, 2013, pp. 3095-3102.

[23] C. Samson, "Mobile robot control, part 2: Control of chained systems and application to path following and time-varying point-stabilization of wheeled vehicles," RR-1994, 1993.

[24] M.-A. Fischler and R.-C. Bolles, "Random Sample Consensus: A Paradigm for Model Fitting with Applications to Image Analysis and Automated Cartography," *Comm. Of the ACM*, 24, 1981, p. 381395.

[25] K. Rabenorosoa, B. Tasca, A. Zerbib, P. Rougeot, N. Andreff, and P. Eakkachai, "SQUIPABOT: a mesoscale parallel robot for a laser phonosurgery," *Int. J. of Optomecha.*, pp. 1–33, 2015.

[26] L. Mattos, N. Deshpande, G. Barresi, L. Guastini, and G. Peretti, "A novel computerized surgeon-machine interface for robot-assisted laser phonomicrosurgery," *Laryngoscope*, vol. 124, p. 1887-1894, 2014.